crystals

MDPI

Article

Effect of Sm^{3+} Doping on Energy Storage Property and Thermal Stability of $BaSn_xTi_{1-x}O_3$ Ceramics

Zhengchao Qin [1,2,3], Zhiyi Wang [1,2,3], Si Gao [1,2,3,*], Hongjuan Zheng [1,2,3], Jin Luo [1,2,3], Yunfei Liu [1,2,3] and Yinong Lyu [1,2,3]

[1] The State Key Laboratory of Materials-Oriented Chemical Engineering, College of Materials Science and Engineering, Nanjing Tech University, Nanjing 210009, China; zcqin@njtech.edu.cn (Z.Q.); zywang@njtech.edu.cn (Z.W.); zhenghj@njtech.edu.cn (H.Z.); jluuky2014@njtech.edu.cn (J.L.); yfliu@njtech.edu.cn (Y.L.); yinonglu@njtech.edu (Y.L.)
[2] Jiangsu National Synergetic Innovation Center for Advanced Materials (SICAM), Nanjing 211816, China
[3] Jiangsu Collaborative Innovation Center for Advanced Inorganic Function Composites, Nanjing 211816, China
* Correspondence: gaosi@njtech.edu.cn

Abstract

Dielectric capacitors have become a key component for energy storage systems, owing to their exceptional power density and swift charge–discharge performance. In a series of lead-free ferroelectric ceramic materials, $BaSn_xTi_{1-x}O_3$ (BTS) received widespread attention due to its unique properties. However, BTS ceramics with high Sn content have high efficiency (η) but low recovery energy storage density (W_{rec}). We incorporated the Sm element into BTS ceramics and aimed to optimize both efficiency and recoverable energy density at moderate Sn content. With the synergistic effect between Sm and Sn, the optimal composition was found at 5% Sn content with 1% low-level Sm dopants, where the energy storage density reached 0.2310 J/cm^3 at 40 kV/cm. Furthermore, the thermal stability of the ceramic was investigated using temperature-dependent dielectric spectroscopy, in situ XRD, and temperature-dependent hysteresis loops. With Sm doping, the fluctuation of W_{rec} decreased from 18.48% to 12.01%. In general, this work not only enhances the understanding of samarium dopants but also proposes strategies for developing lead-free ferroelectric ceramics with superior energy storage properties.

Keywords: BTS; ferroelectrics; energy storage; thermal stability

check for updates

Academic Editor: Daisuke Nakauchi

Received: 5 June 2025
Revised: 23 June 2025
Accepted: 25 June 2025
Published: 26 June 2025

Citation: Qin, Z.; Wang, Z.; Gao, S.; Zheng, H.; Luo, J.; Liu, Y.; Lyu, Y. Effect of Sm^{3+} Doping on Energy Storage Property and Thermal Stability of $BaSn_xTi_{1-x}O_3$ Ceramics. *Crystals* **2025**, *15*, 600. https://doi.org/10.3390/cryst15070600

Copyright: © 2025 by the authors. Licensee MDPI, Basel, Switzerland. This article is an open access article distributed under the terms and conditions of the Creative Commons Attribution (CC BY) license (https://creativecommons.org/licenses/by/4.0/).

1. Introduction

The challenges of an energy crisis and environmental pollution are becoming increasingly prominent, and there is an urgent need to develop high-performance energy storage systems. Dielectric capacitors have gained critical importance, a status attributable to their exceptional power density and swift charge–discharge performance [1–4]. Lead-based ceramics are deployed commercially owing to their remarkable energy storage density. However, the use of lead has caused environmental issues. In the last decade, a series of lead-free ferroelectric ceramic materials have been investigated. Among these materials, barium titanate ($BaTiO_3$, BT) is receiving widespread attention and has been used in various electronics devices, such as electronic ceramics, positive temperature coefficient thermistors, and capacitors.

The key performance of capacitors in practical use is the recovery energy storage density (W_{rec}) and efficiency (η). However, the W_{rec} and η of ferroelectric materials are relatively

low, making it difficult to meet the needs of practical applications [5,6]. To address these limitations, research over the past decade has been focusing on building a morphotropic phase boundary (MPB) by compositional solid substitution [7–10]. For instance, researchers seek to improve performance by substituting at the B-site with elements such as Sn^{4+}, Hf^{4+}, and Zr^{4+} [11–14], where research has shown that these elements have significant advantages in improving the piezoelectricity and energy storage capacity of BT-based ceramics. Sn^{4+} is one of the most effective dopants, while Yao et al. reported the existence of a quasi-four-phase critical point in $BaSn_xTi_{1-x}O_3$ (BTS) system ceramics [15]. Concurrently, extensive research has examined how Sn dopants intrinsically and extrinsically enhance material properties. For instance, Shi et al. investigated $Ba(Ti_{0.8}Sn_{0.2})O_3$ ceramics with high-resolution scanning transmission electron microscopy and observed that the low Sn concentration region formed polar nanoregions (PNRs). The Sn doping manipulated the crystal electronic structure and also increased the dielectric properties in the PNR [16]. Wu et al. observed that with the increase in stannum doping, the domains became smaller and eventually disappeared. The evolution of domain structure leads to polarization anisotropy and also a decrease in domain wall energy, which eventually significantly promote the external piezoelectric response [17]. For now, BTS is used in various potential applications, such as capacitors, thermal radiometers, actuators, and microwave phase shifters [14,18,19].

However, high Sn^{4+} content will lead to a reduction in P_{max}. As a result, although the efficiency is improved, the recovered energy storage density still remains with room for further improvement. Another way to improve BT-based ceramics is doping with elements, such as La^{3+}, Sm^{3+}, Nd^{3+}, etc. [20–23]. Different from the elements that can form a solid perovskite structure, these elements usually only require a few atomic percentages and have various doping effects [24]. On one hand, acceptor doping hinders the movement of the domain walls, making ferroelectrics "hard". On the other hand, doping ferroelectrics with donors "softens" the ceramics because of the internal stress caused by vacancies, and also electrons transfer between the ionized vacancies [25]. Meanwhile, the primary charge compensation mechanism in donor-doped ferroelectrics remains an open question [26,27]. Among these dopants, Sm^{3+} demonstrates distinctive chemical properties: while exerting minimal influence on the phase structure, it significantly enhances the inherent characteristics of the host material [28–32]. Sm appears to exhibit a more pronounced effect compared to other rare-earth elements when employed as a dopant. For instance, Sm^{3+} has been utilized in photocatalysts, optoelectronic displays, and sensors owing to its UV absorption capacity and orange-red luminescence [33]. Moreover, Sm^{3+} is commonly used as an effective luminescent center in the corresponding devices [34].

Nevertheless, systematic investigations into the effects of Sm^{3+} doping on the energy storage properties of $BaTiO_3$-based ceramics remain limited. The physical mechanisms of the effect of Sm^{3+} doping on the ferroelectric properties of BT-based ceramics are also not clear. In this paper, the doping strategy is shown in Figure 1. Due to the decrease in P_{max} caused by excessive Sn content, we chose to incorporate the Sm element into the lower Sn component to further improve η and eventually achieve optimization of both P_{max} and η. We synthesized a series of samples with different Sn contents (2–14%) and Sm doping (0–1.75%) through solid-state reactions and systematically studied the synergistic effect of Sn and Sm on the energy storage performance of $BaTiO_3$ ceramics. The thermal stability property of $Ba_{1-3/2y}Sm_ySn_xTi_{1-x}O_3$ was further investigated.

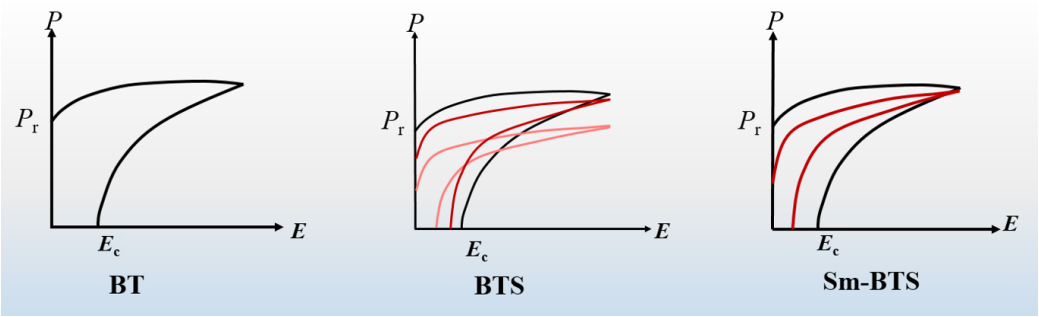


Figure 1. Doping strategy in this paper. The Sm element was incorporated into the lower Sn component to achieve optimization of both P_{max} and η.

2. Materials and Methods

The $Ba_{1-3/2y}Sm_ySn_xTi_{1-x}O_3$ (x = 0.02–0.14, y = 0–0.0175) was prepared by a solid-state reaction method. The raw materials we used are as follows: titanium dioxide (TiO_2, Shanghai Lingfeng Chemical Reagent Co., Ltd.; 99.0%, Shanghai, China), barium carbonate ($BaCO_3$, Sinopharm Chemical Reagent Co., Ltd.; 99.0%, Shanghai, China), tin oxide (SnO_2, Sinopharm Chemical Reagent Co., Ltd.; 99.5%), and samarium oxide (Sm_2O_3, Sinopharm Chemical Reagent Co., Ltd.; 99.9%). The raw powders were precisely weighed and subjected to alcohol-based ball milling for 12 h. After drying, the powders were calcined at 1200 °C for 4 h. The calcined products were re-milled and subsequently pressed into disks using 7 wt% polyvinyl alcohol (PVA) as a binder. Finally, the green bodies were sintered at 1400 °C for 4 h.

The crystalline phase structure of the samples was characterized by X-ray diffraction (XRD; Rigaku SmartLab 9 kW, Tokyo, Japan), and the scanning rate was maintained at 5°/min. Surface morphology analysis was performed using scanning electron microscopy (SEM; JSM-6510, JEOL, Tokyo, Japan). Temperature-dependent dielectric properties were measured from −80 °C to 120 °C using an impedance analyzer (Agilent 4294A, Palo Alto, CA, USA). Hysteresis loops and strain curves were evaluated under an applied electric field of 40 kV/cm via a ferroelectric analyzer (Radiant Technologies Precision Premier II, Albuquerque, NM, USA).

3. Discussion

A series of $Ba_{1-3/2y}Sm_ySn_xTi_{1-x}O_3$ (x = 2–14%, y = 0–1.75%) samples were investigated for their energy storage properties. The properties, for instance, W_d, η, and W_{rec}, were calculated for each component of the ceramics and are shown in Figure 2a–c, respectively. The relationship of the properties is realized with Equations (1)–(3):

$$W_d = \int_0^{P_{max}} EdP \quad (1)$$

$$W_{rec} = \int_{P_r}^{P_{max}} EdP \quad (2)$$

$$\eta = \frac{W_{rec}}{W_d} \times 100\% \quad (3)$$

where W_d stands for the total charged energy, while W_{rec} is the energy that can be discharged. P_{max}, P_r and E stand for the maximum polarization, remnant polarization, and applied electric field, separately, which are the key factors impacting the energy storage properties. Generally speaking, W_d and η are directly connected to a hysteresis loop, since a high W_d is usually proportional to a high P_{max}, while a high η can be directly observed with a "slim"

loop. As indicated in Equation (2), W_{rec} differs from W_d in that W_{rec} is influenced not only by P_{max} but also by P_r. Doping is an exceedingly complex behavior that may alter the lattice parameters, domain structure, and phase composition of the ceramics. However, these changes are often nonlinear, which results in the variation of W_{rec} not exhibiting a monotonic trend [35,36]. Meanwhile, to investigate the effect of changes in these energy storage properties from the chemical doping component, we extracted the hysteresis loops from the binary phase diagrams and show them in Figure 2d–f.

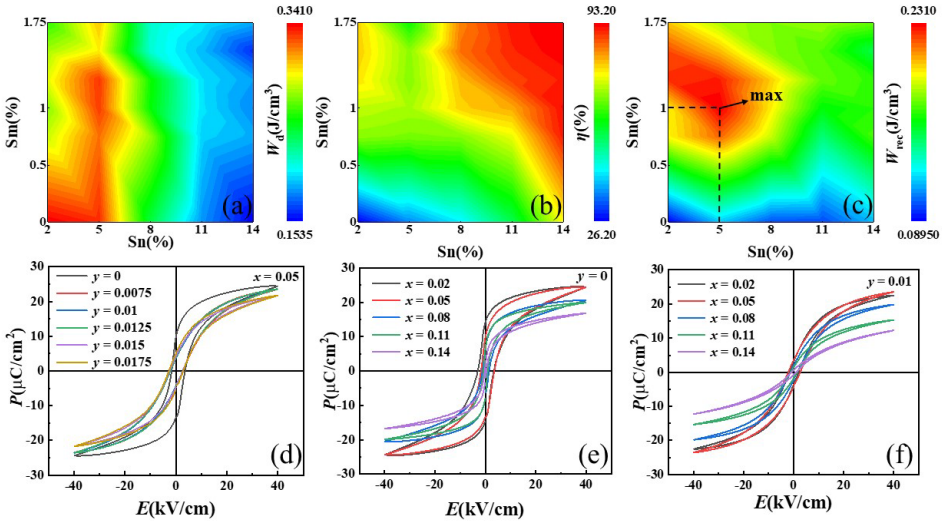


Figure 2. Binary diagrams of $Ba_{1-3/2y}Sm_ySn_xTi_{1-x}O_3$ (x = 2–14%, y = 0–1.75%) ceramics of (**a**) W_d, (**b**) η, (**c**) W_{rec}, and *P-E* loops of $Ba_{1-3/2y}Sm_ySn_xTi_{1-x}O_3$ at 40 kV/cm: (**d**) x = 0.05, (**e**) y = 0, (**f**) y = 0.01.

In general, from these binary phase diagrams, we can find that W_d (shown in Figure 2a) remains unchanged with various Sm contents but decreases as the Sn component increases. As shown in Figure 2e, for pure BTS (namely, y = 0 in $Ba_{1-3/2y}Sm_ySn_xTi_{1-x}O_3$), the *P-E* curves become increasingly "narrow" with the increase in x, and P_{max} values significantly decrease. This trend is identical to previously reported findings [37], where the maximum P_{max} (24.40 μC/cm^2) occurs at x = 0.05. A similar trend is observed for y = 0.01 and x ranging from 0.02 to 0.14 (see Figure 2f). The emergence of this trend may stem from a reduction in the long-range ferroelectric order and the reduction in the polar regions. Meanwhile, η increases with the increase in both Sm and Sn content. Both types of element doping can cause chemical inhomogeneity, leading to the disruption of long-range order. Previous studies have shown that "slim" hysteresis loops arise from the reduction in domain size and the lowered energy barrier for domain switching [17]. For pure BTS, η increases from 26.25% to 75.77%. When Sm is incorporated into a component of 0.01, η ranges from 69.92% to 91.99% (Figure 2f). Overall, η can be enhanced through the synergistic effects of Sn and Sm. When it comes to W_{rec}, we find it does not vary monotonically with either Sm or Sn because W_{rec} is a combination of both W_d and η. W_d decreases while η increases with the Sn component. For a small amount of Sm doping, W_d remains unchanged and η increases. As shown in Figure 2d, η increases from 35.78% to 70.40%, while W_d varies only slightly from 0.3320 J/cm^3 to 0.3281 J/cm^3. In general, we find that W_d can be optimized with the fine-tuning of both the Sm and Sn components. The highest energy storage density is achieved (W_{rec} = 0.2310 J/cm^3 at 40 kV/cm) at x = 0.05 and y = 0.01.

To investigate the microstructure origin of the improvement of energy storage properties, X-ray diffraction was performed on each component of the $Ba_{1-3/2y}Sm_ySn_{0.05}Ti_{0.95}O_3$ ceramics. As shown in Figure 3a, the ceramics display a single perovskite structure with no detectable secondary phase, indicating that Sm is fully incorporated into the perovskite structure. Meanwhile, the (200) peak position shifts to a higher angle (see Figure 2b), which

is attributed to the difference in ionic radii between Sm^{3+} and Ba^{2+}. The ionic radius of Sm^{3+} (approximately 1.24 Å) is smaller than that of Ba^{2+} (approximately 1.61 Å), resulting in a decrease in the average ionic radius at the A site, which theoretically leads to a decrease in the unit cell volume. The interplanar spacing (d) for each composition was calculated using Bragg's law ($n\lambda = 2d \sin\theta$), revealing a decrease from 2.8343 Å to 2.8236 Å. Consequently, the diffraction angle (2θ) should increase, which is consistent with experimental phenomena.

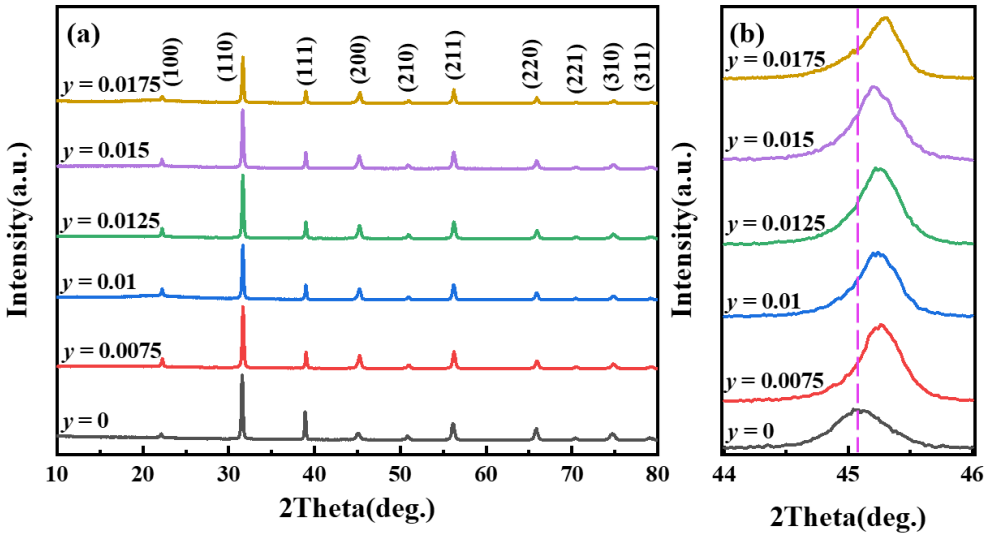


Figure 3. (**a**) XRD patterns (20–80°) of $Ba_{1-3/2y}Sm_ySn_{0.05}Ti_{0.95}O_3$ ceramics and (**b**) magnified views in the intervals of 44–46°.

Figure 4 shows the scanning electron microscope (SEM) images and grain size distribution of $Ba_{1-3/2y}Sm_ySn_{0.05}Ti_{0.95}O_3$ ceramics, as shown in a bar chart in each corresponding figure, respectively. For pure BTS (y = 0), the average grain size is 46.15 μm, calculated using Nano Measurer software (v 1.2). With the doping of Sm, the grain size is significantly reduced. Specifically, when y = 0.01, the average grain size is 1.05 μm. The decrease indicates that the Sm element suppresses grain growth. This phenomenon is commonly observed for Sm doping in various ceramics [38–40]. However, when the concentration of Sm increases, the average grain size remains relatively stable, with values of 1.07 μm, 1.05 μm, 0.84 μm, 0.77 μm, and 0.67 μm corresponding to y = 0.0075, 0.01, 0.0125, 0.015, and 0.0175, respectively (see Figure 4g). Meanwhile, the grain size becomes much more uniform. Numerous studies have systematically investigated the influence of grain size on the properties of ceramic materials, particularly their electronic characteristics. Empirical observations consistently indicate that increased grain dimensions correlate with enhanced saturation polarization and remanent polarization. Notably, contradictory findings have been reported in the literature regarding this relationship [41]. There are also studies that indicated that a reduction in grain size has an optimizing effect on energy storage performance. In our case, the improved performance of this system may be partially attributed to the optimization of the grain size [42–44]. Nevertheless, the exact mechanisms remain unclear and require further investigation. In addition, the density is an important indicator for evaluating the performance of ceramics [45]. We employed the Archimedes drainage method to measure the relative density of the ceramics. With an increasing Sm content, a slight decrease in densification was observed, while all ceramic samples maintained stable relative densities within the range of 94–96%.

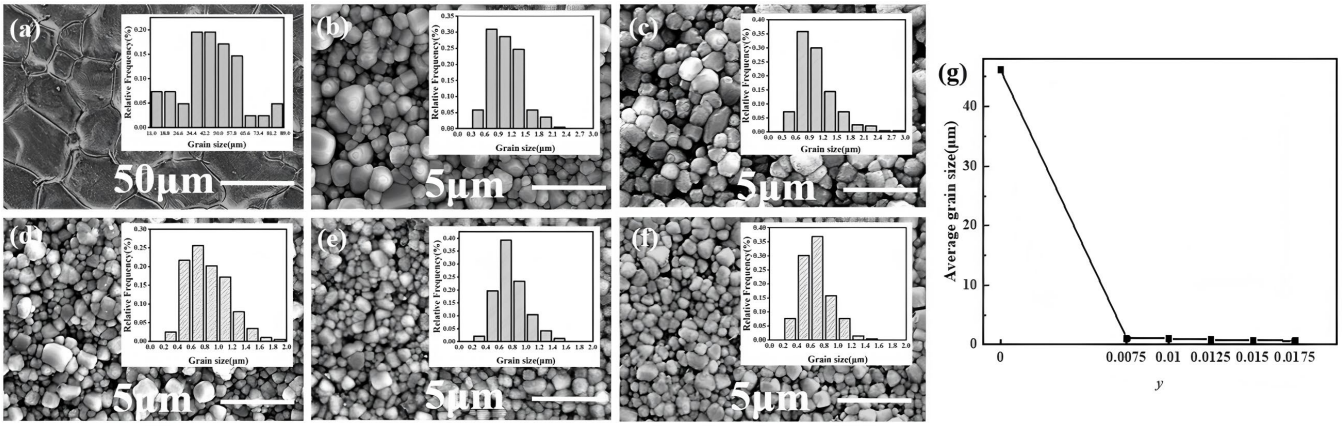


Figure 4. The SEM images of $Ba_{1-3/2y}Sm_ySn_{0.05}Ti_{0.95}O_3$ ceramics sintered with the grain size distribution: (**a**) $y = 0$, (**b**) $y = 0.0075$, (**c**) $y = 0.01$, (**d**) $y = 0.0125$, (**e**) $y = 0.015$, and (**f**) $y = 0.0175$ and (**g**) line graph of average grain size variation.

4. Prospective Studies

In the energy storage application of dielectric ceramic capacitors, thermal stability is an equally important evaluation index for energy storage density and efficiency. Operational heat generation in capacitors compromises dielectric performance, diminishes equipment reliability, and reduces the service life of energy-storage devices. Furthermore, temperature exerts a substantial influence on the energy-storage characteristics of ceramic dielectrics. The observed thermal stability in energy-storage performance originates fundamentally from the material's inherent temperature-resistant dielectric properties. The temperature dependence of the dielectric constant of $Ba_{1-3/2y}Sm_ySn_xTi_{1-x}O_3$ ceramic samples is shown in Figure 5.

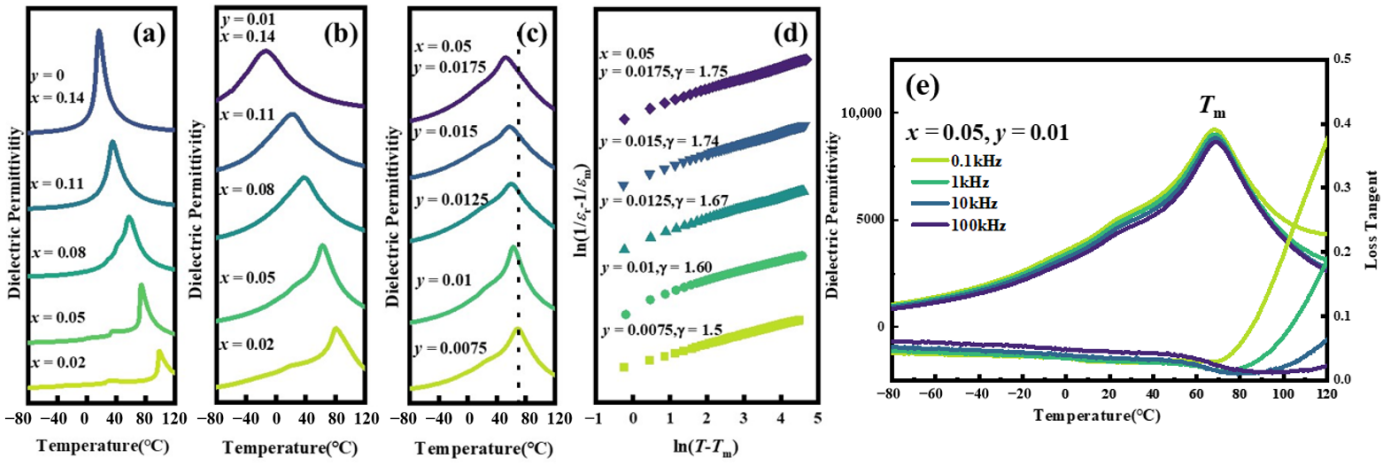


Figure 5. Comparison of temperature-dependent permittivity of $Ba_{1-3/2y}Sm_ySn_xTi_{1-x}O_3$ ceramics at 100 kHz frequency: (**a**) $y = 0$, (**b**) $y = 0.01$, and (**c**) $x = 0.05$, (**d**) relaxation factors of $Ba_{1-3/2y}Sm_ySn_{0.05}Ti_{0.95}O_3$, and (**e**) curves of dielectric constant and dielectric loss of $Ba_{1-3/2y}Sm_ySn_xTi_{1-x}O_3$($x = 0.05$, $y = 0.01$) as a function of temperature at different frequencies.

Many studies have shown that replacing Ti with Sn in BTS systems significantly reduces the Curie temperature [46,47], and our study also obtains a similar result, as shown in Figure 5a. Multiple phase transition peaks gradually merge into a quasi-quadruple point as the Sn content increases, which results in the disappearance of the polarization switching energy barrier and also results in an increase in energy storage properties. When Sm was introduced into the system, a similar trend was observed in the temperature-

dependent dielectric spectrum. As shown in Figure 5b, where y = 0.01, the merging of multiple dielectric peaks and the decrease in Curie temperature can also be observed. However, compared to the component without Sm, its ferroelectric–paraelectric transition peak becomes smoother. By further comparing the effects of Sm doping on the system (Figure 5c), we find that with the increase in Sm content, the ferroelectric–paraelectric transition peak becomes broader, while the dielectric peak intensity is not lost. This indicates that as the Sm content increases, the ferroelectric–paraelectric transition becomes "diffuse", which is consistent with changes in the relaxation factor (γ). The relaxation factor is calculated based on the modified Curie–Weiss law $(1/\varepsilon - 1/\varepsilon_m) = (T - T_m)\hat{}\gamma/C$ (where C is the Curie constant). As shown in Figure 5d, with increasing Sm content, γ increases from 1.5 to 1.75. This phenomenon indicates that the system tends to be more like a relaxor and further proves the effectiveness of Sm element modulation. Especially when x = 0.05 and y = 0.01, the Curie temperature of the system approaches room temperature. This indicates that the system can achieve good room thermal stability through element doping to meet the requirements of the energy storage devices. Meanwhile, this composition exhibits no significant frequency dispersion behavior (see Figure 5e), which is consistent with its relatively small relaxation factor value.

We further explored the thermal stability of $Ba_{1-3/2y}Sm_ySn_xTi_{1-x}O_3$ (x = 0.05 and y = 0.01) ceramics and the microscopic mechanism for the broadening of their dielectric peaks. In situ XRD technology was used to analyze the evolution of the phase structure of the material. The diffraction peaks collected in the temperature range of 20–120 °C are shown in Figure 6a–f. Further, lattice parameters were determined using the Rietveld refinement method with GSAS-II software [48]. During the refinement process, the rhombohedral phase with the space group (PDF#252271, Amm2) structure model [49], the orthorhombic phase with the space group (PDF#252272, P4mm) structure model, and the cubic phase with space group (PDF#56093, Pm3m) were employed [49]. The results of the refinement are shown in Table 1, where all results have $\chi^2 < 3$ and $R_{wp} < 10\%$. When the ambient temperature is 20 °C, the ceramic exhibits a coexistence of orthorhombic and tetragonal phases. When the temperature rises to 40 °C, the orthorhombic phase volume fraction decreases (from 38.70% to 15.37%) and the tetragonal phase volume fraction increases (from 61.30% to 84.63%). This indicates that the ceramic undergoes an O-T phase transition. When the temperature is between 60 and 80 °C, the ceramic undergoes a phase transition from the tetragonal to the cubic phase. As the temperature continues to increase, it transforms into the cubic phase. The trend of multiphase changes indicates that after Sm doping, $Ba_{1-3/2y}Sm_ySn_xTi_{1-x}O_3$ ceramics undergo a relatively gentle phase transition process when the temperature changes, which is in line with the behavior of the temperature-dependent permittivity of this component shown in Figure 5. Meanwhile, these phase transition characteristics also indicate that the material may have good thermal stability.

Hysteresis loops were tested for both Sm-doped components (y = 0.01) and undoped components (y = 0), in the temperature range of 20–80 °C. As shown in Figure 7, when the temperature rises, the maximum polarization intensity (P_{max}) decreases for both components. This may be due to thermal disturbance, which hinders the dipole orientation arrangement inside the material and thereby weakens the polarization ability. When x = 0.05 and y = 0, the fluctuation amplitude of W_{rec} within this temperature range was calculated to be 18.48% (from 0.1188 J/cm^3 to 0.0968 J/cm^3, see Figure 7c). When x = 0.05 and y = 0.01, the fluctuation amplitude of W_{rec} is 12.01% (from 0.2310 J/cm^3 to 0.2033 J/cm^3). This indicates that doping Sm in BTS can optimize the thermal stability of the system.

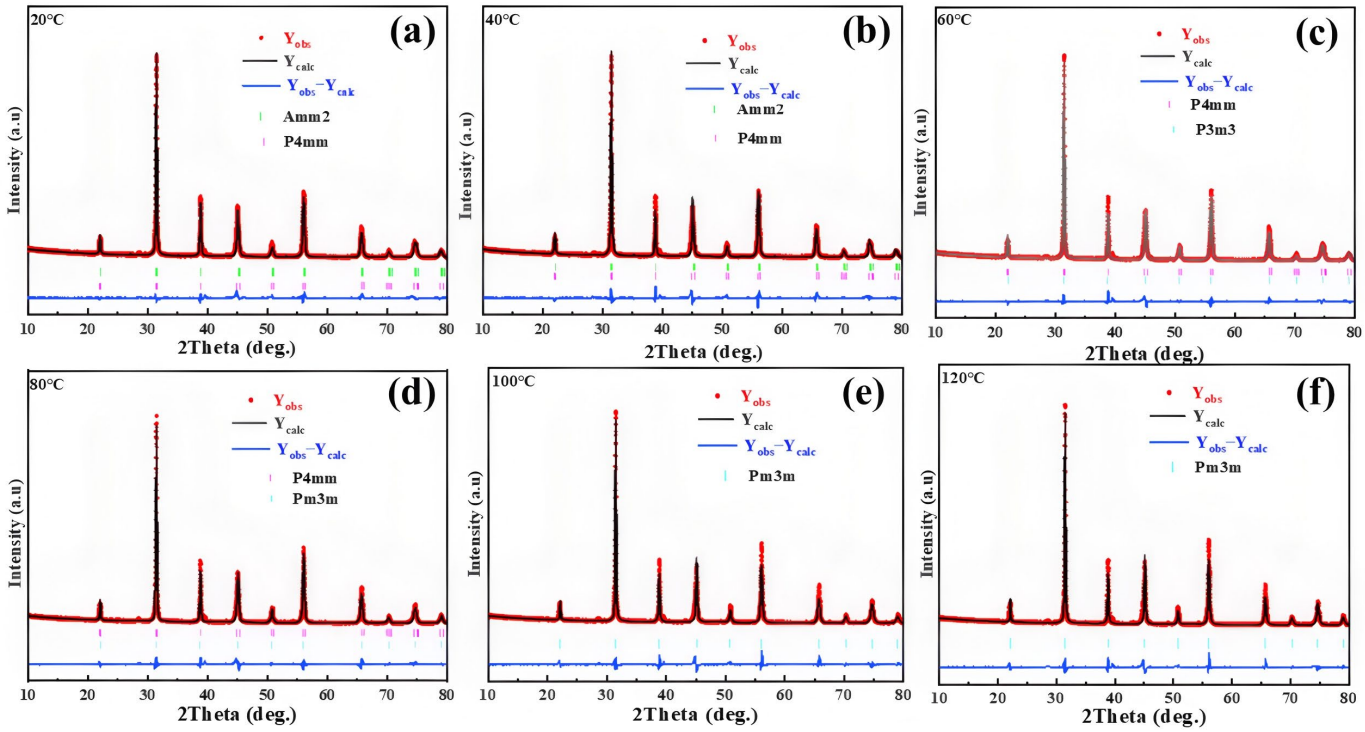


Figure 6. Rietveld-refined XRD patterns of $Ba_{1-3/2y}Sm_ySn_xTi_{1-x}O_3$($x$ = 0.05, y = 0.01) ceramics at different temperatures: (**a**) 20 °C, (**b**) 40 °C, (**c**) 60 °C, (**d**) 80 °C, (**e**) 100 °C, and (**f**) 120 °C.

Table 1. Lattice parameters, cell volume, and reliability factors of $Ba_{1-3/2y}Sm_ySn_xTi_{1-x}O_3$($x$ = 0.05 and y = 0.01) ceramics.

T (°C)	Space Group	Unit Cell Parameters				Phase Fraction (%)	χ^2	R_{wp} (%)
		a(Å)	b(Å)	c(Å)	V(Å^3)			
20	Amm2	4.0504	4.0399	5.6423	92.326	38.70	2.41	6.5
	P4mm	4.0230	-	4.0050	64.819	61.30		
40	Amm2	4.0475	4.0210	5.6440	91.855	15.37	2.26	8.3
	P4mm	4.0231	-	4.0041	64.806	84.63		
60	P4mm	4.0120	4.0120	4.0266	64.813	35.74	2.24	6.2
	Pm3m	4.0511	-	-	64.484	64.26		
80	P4mm	4.0140	-	4.0296	64.923	12.19	2.29	6.5
	Pm3m	4.0488	-	-	66.37	87.81		
100	Pm3m	4.0201	-	-	64.967	100	2.33	8.2
120	Pm3m	4.0195	-	-	64.939	100	2.68	7.8

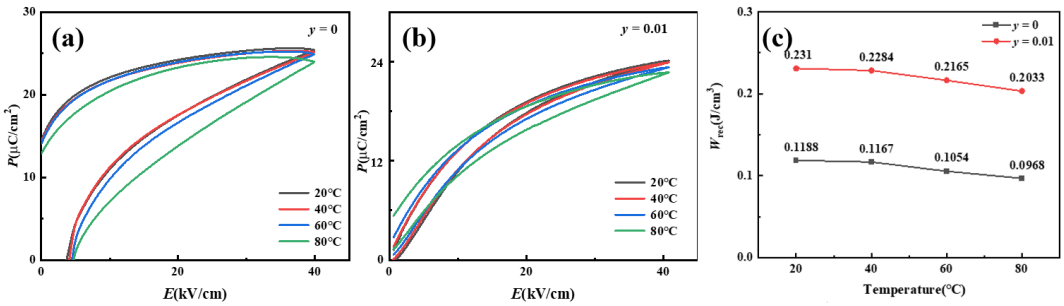


Figure 7. Temperature dependence of P-E hysteresis loops of $Ba_{1-3/2y}Sm_ySn_{0.05}Ti_{0.95}O_3$: (**a**) y = 0, (**b**) y = 0.01 and (**c**) the line graph of the value of W_{rec} in relation to temperature changes.

5. Conclusions

In this study, the energy storage performance and thermal stability of Sm-doped BTS ceramics were investigated. To solve the problem that P_{max} decreases in BTS ceramics with high Sn content, we incorporate the Sm element into BTS ceramics with low Sn content. The results indicate that Sm doping can improve the relaxor behavior of the material and effectively enhance energy storage efficiency without significantly reducing P_{max}. Binary diagrams of energy storage performance were drawn, with different Sm and Sn components. The optimal component for the synergistic effect of Sm and Sn was found to be 5% Sn content with 1% low-level Sm dopants, with an energy storage density of 0.2310 J/cm^3 at 40 kV/cm and an efficiency of 70.40%. Furthermore, the thermal stability of the ceramic was investigated using temperature dielectric spectroscopy, in situ XRD, and temperature-dependent hysteresis loops. Compared to undoped BTS ceramic, the fluctuation of W_{rec} decreases from 18.48% to 12.01%. These results indicate that the incorporation of the Sm element effectively improves the energy storage performance and thermal stability of BTS ceramics, which has practical significance for dielectric capacitors. This study elucidates the role of samarium dopants and proposes novel design strategies for developing lead-free ferroelectric ceramics exhibiting enhanced energy-storage performance.

Author Contributions: Conceptualization, S.G.; Methodology, Z.Q.; Software, Z.Q. and Z.W.; Validation, S.G. and Z.Q.; Formal Analysis, Z.Q. and Z.W.; Investigation Z.Q. and H.Z.; Resources, J.L., Y.L. (Yunfei Liu) and Y.L. (Yinong Lyu); Writing—Original Draft, Z.W.; Writing—Review and Editing, S.G.; Supervision, S.G., Y.L. (Yunfei Liu) and Y.L. (Yinong Lyu); Project Administration, S.G.; Funding Acquisition, S.G., H.Z. and J.L.; All authors have read and agreed to the published version of the manuscript.

Funding: This research was funded by the National Natural Science Foundation of China (Grant No. 11904164, 51902155, 52202137), the Natural Science Foundation of Jiangsu Province (Grant No. BK20210187).

Data Availability Statement: The original contributions presented in this study are included in the article. Further inquiries can be directed to the corresponding author.

Conflicts of Interest: The authors declare no conflicts of interest.

References

1. Li, J.; Shen, Z.; Chen, X.; Yang, S.; Zhou, W.; Wang, M.; Wang, L.; Kou, Q.; Liu, Y.; Li, Q.; et al. Grain-orientation-engineered multilayer ceramic capacitors for energy storage applications. *Nat. Mater.* **2020**, *19*, 999–1005. [CrossRef] [PubMed]
2. Han, S.; Kim, J.S.; Park, E.; Meng, Y.; Xu, Z.; Foucher, A.C.; Jung, G.Y.; Roh, I.; Lee, S.; Kim, S.O.; et al. High energy density in artificial heterostructures through relaxation time modulation. *Science* **2024**, *384*, 312–317. [CrossRef] [PubMed]
3. Zhang, M.; Lan, S.; Yang, B.B.; Pan, H.; Liu, Y.Q.; Zhang, Q.H.; Qi, J.L.; Chen, D.; Su, H.; Yi, D.; et al. Ultrahigh energy storage in high-entropy ceramic capacitors with polymorphic relaxor phase. *Science* **2024**, *384*, 185–189. [CrossRef]
4. Gao, Y.; Qiao, W.; Lou, X.; Song, Z.; Zhu, X.; He, L.; Yang, B.; Hu, Y.; Shao, J.; Wang, D.; et al. Ultrahigh energy storage in tungsten bronze dielectric ceramics through a weakly coupled relaxor design. *Adv. Mater.* **2023**, *36*, 2310559. [CrossRef]
5. Li, D.; Zhou, D.; Wang, D.; Zhao, W.; Guo, Y.; Shi, Z.; Zhou, T.; Sun, S.-K.; Singh, C.; Trukhanov, S.; et al. Lead-free relaxor ferroelectric ceramics with ultrahigh energy storage densities via polymorphic polar nanoregions design. *Small* **2022**, *19*, 2206958. [CrossRef]
6. Hu, Q.; Tian, Y.; Zhu, Q.; Bian, J.; Jin, L.; Du, H.; Alikin, D.O.; Shur, V.Y.; Feng, Y.; Xu, Z.; et al. Achieve ultrahigh energy storage performance in $BaTiO_3$-$Bi(Mg_{1/2}Ti_{1/2})O_3$ relaxor ferroelectric ceramics via nano-scale polarization mismatch and reconstruction. *Nano Energy* **2019**, *67*, 104264. [CrossRef]
7. Nayak, R.L.; Dash, S.S.; Zhang, Y.; Sahoo, M.P.K. Enhanced dielectric, thermal stability, and energy storage properties in compositionally engineered lead-free ceramics at morphotropic phase boundary. *Ceram. Int.* **2021**, *47*, 17220–17233. [CrossRef]
8. Liu, T.; Yan, B.; Ma, J.; He, Q.; An, L.; Chen, K. Enhanced energy storage properties in BNT-based ceramics with a morphotropic phase boundary modified by $Sr(Mg_{1/3}Nb_{2/3})O_3$. *J. Mater. Chem. C* **2023**, *11*, 15294–15302. [CrossRef]

9. Neha; Richa, P.; Manoj, B.; Parveen, K.; Rajesh Kumar, M.; Chandra, P. Improved dielectric and energy storage properties in (1-x)$BaTi_{0.80}Zr_{0.20}O_3$-$xBa_{0.70}Ca_{0.30}Ti_{0.99}Fe_{0.01}O_3$ ceramics near morphotropic phase boundary. *Mater. Lett.* **2022**, *318*, 132126. [CrossRef]
10. Sharma, S.; Nandan, R.; Malhotra, P.; Kumar, S.; Kumar, R.; Negi, N.S. Morphotropic phase boundary evolution with synergistic effect of sintering temperature to improve electrocaloric and energy storage performances of lead-free $Ba_{0.95}Ca_{0.05}Sn_{0.09}Ti_{0.91}O_3$ (BCST) ceramic. *J. Energy Storage* **2024**, *99*, 113295. [CrossRef]
11. Co, K.; Khassaf, H.; Alpay, S.P. Electrocaloric and pyroelectric properties of barium zirconate titanate. *J. Appl. Phys.* **2020**, *127*, 174102. [CrossRef]
12. Liu, G.; Yu, W.; Wang, Y.; Feng, H.; Hao, M.; Wu, G.; Li, Q.; Yu, K.; Fan, B.; Jin, L.; et al. Electrocaloric effect of $(Ba_{1-x}Sr_x)(Hf_xTi_{1-x})O_3$ lead-free ferroelectric ceramics with phase structure regulation. *Ceram. Int.* **2023**, *49*, 34387–34396. [CrossRef]
13. Wei, X.; Feng, Y.; Wan, X.; Yao, X. Evolvement of dielectric relaxation of barium stannate titanate ceramics. *Ceram. Int.* **2004**, *30*, 1397–1400. [CrossRef]
14. Zhang, H.; Giddens, H.; Saunders, T.G.; Palma, M.; Abrahams, I.; Yan, H.; Hao, Y. Microwave tunability in tin substituted barium titanate. *J. Eur. Ceram. Soc.* **2023**, *44*, 1627–1635. [CrossRef]
15. Yonggang, Y.; Chao, Z.; Duchao, L.; Dong, W.; Haijun, W.; Yaodong, Y.; Xiaobing, R. Large piezoelectricity and dielectric permittivity in $BaTiO_3$-$xBaSnO_3$ system: The role of phase coexisting. *EPL* **2012**, *98*, 27008. [CrossRef]
16. Shi, T.; Xie, L.; Gu, L.; Zhu, J. Why Sn doping significantly enhances the dielectric properties of $Ba(Ti_{1-x}Sn_x)O_3$. *Sci. Rep.* **2015**, *5*, 8606. [CrossRef]
17. Wu, B.; Zheng, H.; Wu, Y.-Q.; Huang, Z.; Thong, H.-C.; Tao, H.; Ma, J.; Zhao, C.; Xu, Z.; Liu, Y.-X.; et al. Origin of ultrahigh-performance barium titanate-based piezoelectrics: Stannum-induced intrinsic and extrinsic contributions. *Nat. Commun.* **2024**, *15*, 7700. [CrossRef]
18. Marković, S.; Jovalekić, Č.; Veselinović, L.; Mentus, S.; Uskoković, D. Electrical properties of barium titanate stannate functionally graded materials. *J. Eur. Ceram. Soc.* **2009**, *30*, 1427–1435. [CrossRef]
19. Manisha, K.; Sarun, M. High-temperature impedance, modulus spectroscopy, and conductivity study of Nd modified barium stannate titanate electroceramics. *ECS Trans.* **2022**, *107*, 11497. [CrossRef]
20. Ben Mrad, M.; Hannachi, R.; Dammak, M.; Abdelmoula, N.; Zghal, S.; Khemakhem, H. Zirconium and lanthanide effects on the structural, dielectric and optical properties of $Na_{0.8}Ba_{0.2}Nb_{0.8}Ti_{0.2}O_3$ ferroelectric ceramic. *Mater. Today Commun.* **2020**, *24*, 101223. [CrossRef]
21. Lou, Y.; Chen, Y.; Gu, Z.; Qiu, Q.; Shi, C.; He, L.; Xing, Y.; Peng, J.; Li, H.; Chu, Y.; et al. Enhancement of Photoluminescence and Anomalous Thermal Quenching Behavior of Er/Yb/Zr co-doped $BaTiO_3$ Ceramic. *Ceram. Int.* **2021**, *47*, 18866–18874. [CrossRef]
22. Bajpai, K.K.; Sreenivas, K.; Thakur, O.P.; James, A.R.; Shukla, A.K. Influence of Cd doping on the electro-strain of barium zirconate titanate ceramics. *Ceram. Int.* **2017**, *43*, 1963–1967. [CrossRef]
23. Kang, N.; Kim, M.; Song, H.; Ryu, J. Effects of Sm2O3 addition on the dielectric and energy storage properties of BaTiO3 ceramics. *J. Korean Ceram. Soc.* **2024**, *61*, 1070–1078. [CrossRef]
24. Li, Y.-X.; Yao, X.; Wang, X.-S.; Hao, Y.-B. Studies of dielectric properties of rare earth (Dy, Tb, Eu) doped barium titanate sintered in pure nitrogen. *Ceram. Int.* **2012**, *38*, 29–32. [CrossRef]
25. Li, Z.; Yu, J.; Hao, S.; Janolin, P.-E. Enhancing properties of lead-free ferroelectric $BaTiO_3$ through doping. *J. Eur. Ceram. Soc.* **2022**, *42*, 4693–4701. [CrossRef]
26. Cuiying, M.; Huiling, D.; Jia, L.; Xian, D.; Danni, F. Charge compensation mechanisms of BaTiO3 ceramics co-doped with La2O3 and Bi2O3. *Ceram. Int.* **2021**, *48*, 5428–5433. [CrossRef]
27. Pandey, A.H.; Gupta, S.M. Role of charge compensation mechanism on phase formation, dielectric and ferroelectric properties in aliovalent Gd3+ ion modified PbMg1/3Nb2/3O3 ceramics. *Mater. Sci. Eng.* **2020**, *253*, 114495. [CrossRef]
28. Jing, L.; Li, J.; Ye, T.; Chao, C.; Yu, L.; Qingyuan, H.; Chao, L.; Xiaoyong, W.; Haixue, Y. Enhanced energy storage performance under low electric field in Sm^{3+} doped $AgNbO_3$ ceramics. *J. Mater.* **2021**, *8*, 266–273. [CrossRef]
29. Jiaqi, C.; Ping, P.; Yongde, L.; Hengchang, N.; Genshui, W. Electrostrain optimization of bismuth sodium titanate-based ceramics by Sm doping. *J. Am. Ceram. Soc.* **2025**, *108*, 20415. [CrossRef]
30. Qiaoli, L.; Junwei, L.; Yongfu, L.; Meijing, W.; Weihao, W.; Dayong, L. Structure-dependent dielectric relaxations in Sm-doped $BaTiO_3$ ceramics. *Ceram. Int.* **2021**, *47*, 34042–34049. [CrossRef]
31. Wang, C.; Li, Y.; Sun, P.; Yang, S.; Zhang, H.; Chen, Q. Electrical transport properties of Sm-doped $La_{0.7}Ca_{0.3}MnO_3$ polycrystalline ceramics. *Ceram. Int.* **2021**, *47*, 25281–25286. [CrossRef]
32. Zhou, Y.; Ye, F.; Cai, Y.; Li, H. Enhanced dielectric and relaxation properties in Sm^{3+} doped KNNT ceramics. *Ceram. Int.* **2024**, *50*, 27596–27606. [CrossRef]
33. Guan, P.; Zhang, Y.; Yang, J.; Zheng, M. Effect of Sm^{3+} doping on ferroelectric, energy storage and photoluminescence properties of $BaTiO_3$ ceramics. *Ceram. Int.* **2022**, *49*, 11796–11802. [CrossRef]

34. Nikolić, M.G.; Jovanović, D.J.; Đorđević, V.; Antić, Ž.; Krsmanović, R.M.; Dramićanin, M.D. Thermographic properties of Sm3+-doped GdVO4phosphor. *Phys. Scr.* **2012**, *2012*, T149. [CrossRef]
35. Benyoussef, M.; Zannen, M.; Belhadi, J.; Manoun, B.; Dellis, J.-L.; El Marssi, M.; Lahmar, A. Dielectric, ferroelectric, and energy storage properties in dysprosium doped sodium bismuth titanate ceramics. *Ceram. Int.* **2018**, *44*, 19451–19460. [CrossRef]
36. Li, Y.; Hu, T.; Chen, X.; Xie, J.; Shi, Y. Achieving high energy storage performance in PbHfO3-based antiferroelectric ceramics by Sr element doping. *J. Alloys Compd.* **2024**, *994*, 174651. [CrossRef]
37. Ma, X.; Shi, W.; Yang, Y.; Alikin, D.O.; Shur, Y.Y.; Gao, J.; Wei, X.; Liu, G.; Du, H.; Jin, L. Giant electrocaloric effect and high-field electrostrictive properties in $Ba(Ti_{1-x}Sn_x)O_3$ ceramics. *Ceram. Int.* **2023**, *49*, 18517–18524. [CrossRef]
38. Dong, S.; Guo, F.; Zhou, H.; Long, W.; Fang, P.; Li, X.; Xi, Z. Phase structures and electrical properties of Sm doped PSN-PMN-PT ceramics. *J. Alloys Compd.* **2021**, *881*, 160621. [CrossRef]
39. Bag, S.; Behera, B. Transport phenomena and conductivity mechanism in Sm doped $Bi_4V_{2-x}SmxO_{11}$ ceramics. *J. Sci. Adv. Mater. Dev.* **2016**, *108*, 20415. [CrossRef]
40. Li, Q.; Bao, S.; Liu, Y.; Li, Y.; Jing, Y.; Li, J. Influence of lightly Sm-substitution on crystal structure, magnetic and dielectric properties of $BiFeO_3$ ceramics. *J. Alloys Compd.* **2016**, *682*, 672–678. [CrossRef]
41. Ghayour, H.; Abdellahi, M. A brief review of the effect of grain size variation on the electrical properties of $BaTiO_3$-based ceramics. *Powder Technol.* **2016**, *292*, 84–93. [CrossRef]
42. Wang, Z.; Bin, C.; Zheng, S.; Wang, J. Effect of grain size and grain boundary on the energy storage performance of polycrystalline ferroelectrics. *Appl. Phys. Lett.* **2024**, *125*, 152903. [CrossRef]
43. Yangfei, G.; Xiaopei, Z.; Bian, Y.; Peng, S.; Ruirui, K.; Ye, Y.; Qida, L.; Ming, W.; Jinghui, G.; Xiaojie, L. Grain size modulated (Na0.5Bi0.5)0.65Sr0.35TiO3-based ceramics with enhanced energy storage properties. *Chem. Eng. J.* **2021**, *433*, 133584. [CrossRef]
44. Wang, X.; Huan, Y.; Zhao, P.; Liu, X.; Wei, T.; Zhang, Q.; Wang, X. Optimizing the grain size and grain boundary morphology of $(K,Na)NbO_3$-based ceramics: Paving the way for ultrahigh energy storage capacitors. *J. Mater.* **2021**, *7*, 780–789. [CrossRef]
45. Klym, H.; Karbovnyk, I.; Luchechko, A.; Kostiv, Y.; Pankratova, V.; Popov, A.I. Evolution of Free Volumes in Polycrystalline BaGa2O4 Ceramics Doped with Eu3+ Ions. *Crystals* **2021**, *11*, 1515. [CrossRef]
46. Ansari, M.A.; Sreenivas, K. Effects of disorder activated scattering and defect-induced phase on the ferroelectric properties of $BaSn_xTi_{1-x}O_3$ ($0 \leq x \leq 0.28$) ceramics. *Ceram. Int.* **2019**, *45*, 20738–20749. [CrossRef]
47. Xiaoyong, W.; Yujun, F.; Xi, Y. Dielectric relaxation behavior in barium stannate titanate ferroelectric ceramics with diffused phase transition. *Appl. Phys. Lett.* **2003**, *83*, 2031–2033. [CrossRef]
48. Zaitouni, H.; Hajji, L.; Mezzane, D.; Choukri, E.; Gagou, Y.; Hoummada, K.; Charai, A.; Alimoussa, A.; Rožič, B.; El Marssi, M.; et al. Structural, dielectric, ferroelectric and tuning properties of Pb-free ferroelectric $Ba_{0.9}Sr_{0.1}Ti_{1-x}Sn_xO_3$. *Ceram. Int.* **2020**, *46*, 27275–27282. [CrossRef]
49. Kalyani, A.K.; Krishnan, H.; Sen, A.; Senyshyn, A.; Ranjan, R. Polarization switching and high piezoelectric response in Sn-modified $BaTiO_3$. *Phys. Rev. B* **2015**, *91*, 024101. [CrossRef]

Disclaimer/Publisher's Note: The statements, opinions and data contained in all publications are solely those of the individual author(s) and contributor(s) and not of MDPI and/or the editor(s). MDPI and/or the editor(s) disclaim responsibility for any injury to people or property resulting from any ideas, methods, instructions or products referred to in the content.